

Supplementary Materials for

Defects and plasticity in ultrastrong supercrystalline nanocomposites

D. Giuntini*, S. Zhao, T. Krekeler, M. Li, M. Blankenburg, B. Bor, G. Schaan, B. Domènech, M. Müller,
I. Scheider, M. Ritter, G. A. Schneider

*Corresponding author. Email: diletta.giuntini@tuhh.de

Published 8 January 2021, *Sci. Adv.* 7, eabb6063 (2021)
DOI: 10.1126/sciadv.abb6063

This PDF file includes:

Texts S1 to S7
Figs. S1 to S9
Table S1

Supplementary Materials

1. Superlattice parameters

Data on the iron oxide nanoparticles size and on the supercrystalline lattice were obtained via small-angle x-ray scattering (SAXS). Fig. S1 shows the scattering curve of the initial suspension of functionalized nanoparticles (A), their size distribution (B), and the scattering curve of the supercrystalline materials, before and after heat treatment (C). As reported in the main article, the nanoparticle radius is found to be 7.9 ± 1.3 nm. This is assumed to be the radius of the iron oxide core, not inclusive of the oleic acid functionalization, but the option that such a value is a slight overestimation of the core radius should be kept in mind. The FCC superlattice parameter is 25.7 and 24.5 nm for the material before and after heat treatment, respectively.

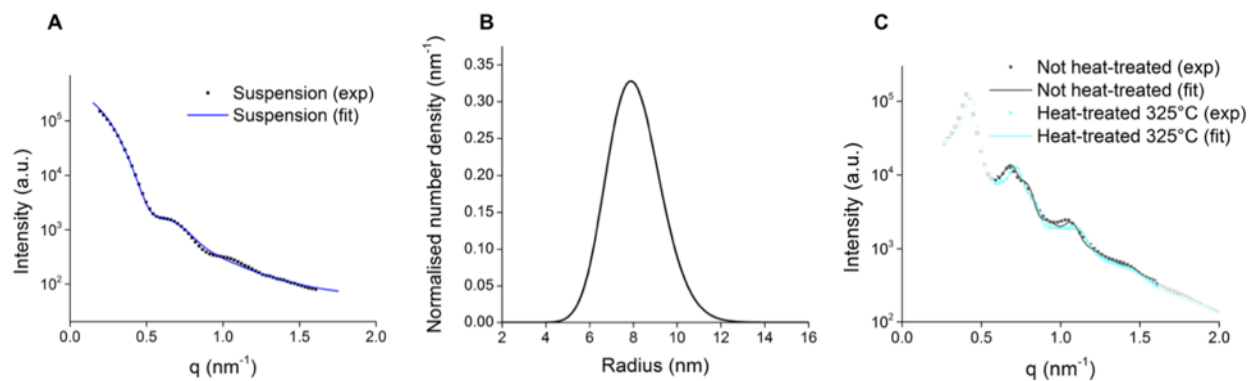


Fig. S1. Nanoparticles' size and superlattice characterization via SAXS.

(A) Scattering curve of the suspension of functionalized nanoparticles (dotted line: experimental data, continuous line: fit).

(B) Nanoparticle size distribution as obtained from the suspension's SAXS data (number density-based fit).

(C) Scattering curve of the supercrystalline materials, before and after heat treatment (dotted line: experimental data, continuous line: fit, based on the highlighted region, $q = 0.6$ - 1.6 nm^{-1} , to be more sensitive to the shift of the 200 and 311 reflections).

2. Low angle grain boundary evaluation

As reported in the main text, for orientation mismatches among neighboring grains (supercrystalline domains) lower than 15° , the low-angle grain boundary model can be applied. The distance among edge dislocations D and the mismatch angle θ are defined as in Fig. S2. Measured D values are 87, 95, 108, 147, 167, 190 and 257 nm (average ~ 150 nm), while θ was measured at different locations on TEM micrographs, and resulted in an average of 6° (0.11 rad). Given D and θ , a Burgers vector of modulus $b = D \cdot \theta = 15.7$ nm is found.

The modulus of the Burgers vector can also be identified via direct measurement of the lattice mismatch surrounding the dislocation core in the micrographs (see scheme in Fig. 1C). This can only yield an approximate value ($b \sim 14.3$ nm) with the given resolution of the TEM micrographs.

The micrograph's zone axis, $[11\bar{2}]$, does not allow clear imaging of edge-on dislocations and in turn drawing straightforward conclusions on the dislocations type. The dislocation line or Burgers vector can be inclined with respect to the image plane, or the dislocations can be identified as Frank partials of $\frac{a}{3}\langle 111 \rangle$ type. These options are compatible with the above considerations on the Burgers vector's modulus.

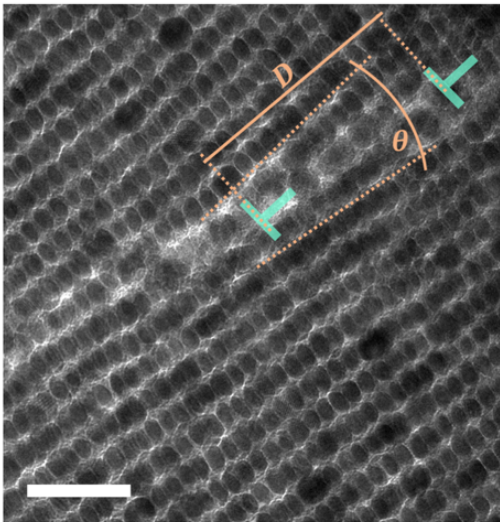


Fig. S2. Low-angle grain boundary. Definition of geometrical parameters of low-angle grain (inter-supercrystalline) boundary (D , distance among boundary edge dislocations, and θ , orientation mismatch across the boundary) on TEM micrograph example. Scale bar is 50 nm.

3. Pile-ups' volume estimation and material compaction

The volume of material displaced by the indenting tips was calculated as the volume of a pyramid with base area measured via image analysis (ImageJ) on SEM micrographs, and height given by the residual indentation depth after tip retraction (extracted from nanoindentation curves), to rule out the effect of elastic recovery and avoid relying simply on the indenting tips' area functions, which often lead to inaccurate values. The indents and data used for these calculations are shown in Fig. S3. The pile-ups' volume around the indents was evaluated by approximating each pile-up from AFM data (Fig. S4), as illustrated in Table S1. Several geometries were attempted to approximate the volumes of the pile-ups, all leading to very similar results. The resulting indented and pile-ups' volumes are summarized in Table S1, together with their ratio, which serves as indicator of material compaction. Note that, because of the different times at which nanoindentation and AFM data were collected, some extent of time-dependent deformation could be captured only in the AFM data. This effect, and the approximated pile-up shapes, can potentially lead to slight underestimations of the ratios given in Table S1, so the given ratios should be considered as indications of trends more than exact values.

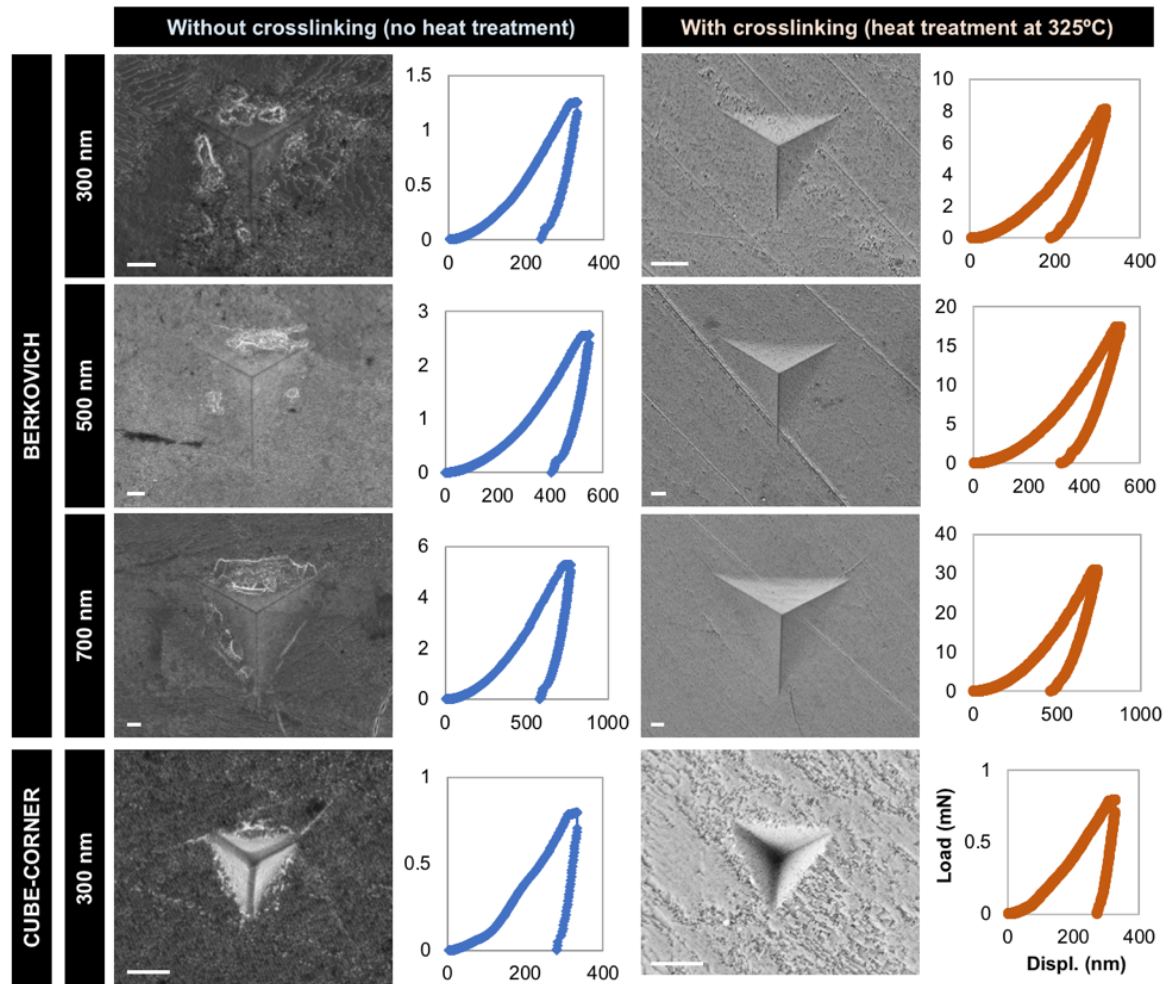


Fig. S3. Indents. Nanoindentation load-displacement curves and corresponding indents' SEM micrographs used for the calculation of the volume displaced by the indenting tips. Note the more marked irregularities in the curves relative to the cube-corner tip, correlated with material cracking. Selected SEM Micrographs reproduced with permission from (7). Scale bars are 500 nm.

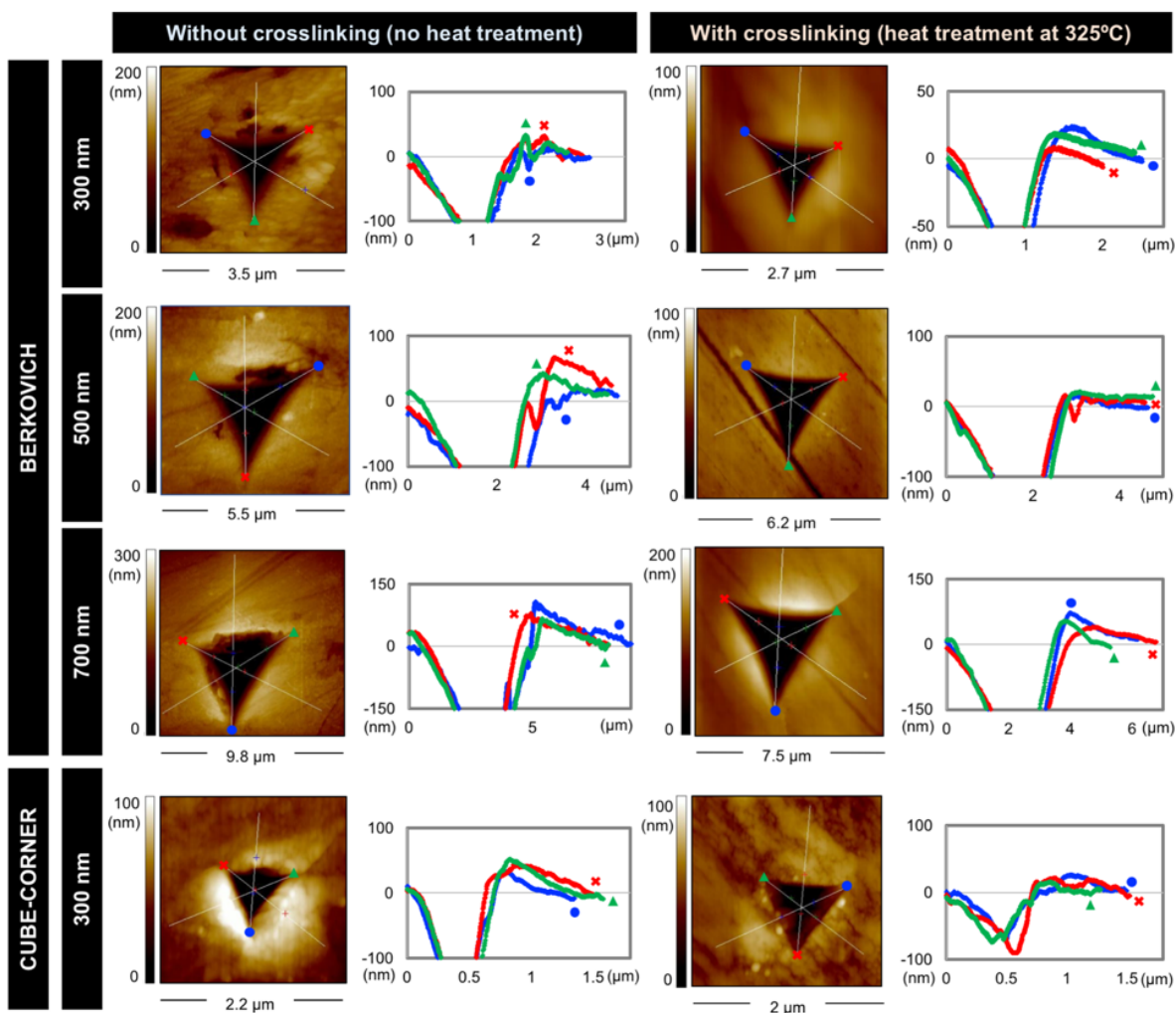


Fig. S4. Pile-ups. AFM-obtained topography maps and profiles from which pile-ups' volumes were estimated.

Material	Without crosslinking				With crosslinking				
	Berkovich		CC		Berkovich		CC		
Depth (nm)	300	500	700	300	300	500	700	300	
V_{ind} (μm^3)	0.16	0.46	1.76	0.03	0.12	0.49	1.55	0.03	
$V_{pileups}$ (μm^3)	0.05	0.33	1.35	0.02	0.01	0.07	0.56	0.02	
$V_{pileups}/V_{ind}$	0.33	0.73	0.77	0.57	0.10	0.13	0.36	0.55	

Table 1. Pile-ups/indented volume ratio. Volumes displaced by indenting tips (Berkovich and cube-corner, CC) and of the corresponding pile-ups for indents of varying depth in supercrystalline nanocomposites without and with crosslinking of the organic ligands, with scheme of the selected pile-ups' approximated geometry.

4. Estimation of unbound oleic acid content

The distribution of the oleic acid phase within the superlattice was evaluated by comparing the oleic acid volume fractions resulting from small-angle x-ray scattering (SAXS) data and from thermogravimetric analysis (TGA). It was assumed that each iron oxide nanoparticle is covered by a uniform oleic acid shell, with varying thickness depending on organic chains interdigitation, potential bending and crosslinking, and calculated from SAXS data.

From SAXS data, we have a superlattice constant a of 25.7 nm for the non-crosslinked material, and 24.5 nm for the crosslinked one. Given the radius of the iron oxide nanoparticles (7.9 nm), inter-particle distances of 2.4 nm and 1.5 nm are found for the two materials, respectively, corresponding to oleic acid “shell” thicknesses of ~ 1.2 and ~ 0.8 nm. The overall volume occupied by this oleic acid layer in the two materials thus amounts to 4308 nm³ for the non-crosslinked material, and 2629 nm³ for the crosslinked one. The total volume of each unit cell is calculated as a^3 , is 16975 nm³ before crosslinking and 14706 nm³ afterwards. This means that the oleic acid layer anchored to the iron oxide nanoparticles occupies 25% of the overall unit cell volume before heat treatment, and 18% afterwards.

On the other hand, TGA (see Fig. S5) of the initial iron oxide-oleic acid suspension reveals an oleic acid content of ~ 7.5 wt% before heat treatment at 325°C, and ~ 3.5 wt% afterwards. The temperature interval of interest for detection of oleic acid desorption is 150-450 °C. Based on a density of iron oxide $\rho_{\text{Fe}_3\text{O}_4} = 5.24$ g/cm³ and of oleic acid $\rho_{\text{OA}} = 0.89$ g/cm³, this results in ~ 32 vol% and ~ 18 vol% for non-heat-treated and heat-treated materials, respectively ($\text{vol}\% = \text{wt}\% / [\text{wt}\% + (1 - \text{wt}\%) \rho_{\text{Fe}_3\text{O}_4} / \rho_{\text{OA}}]$) (4,7). We can therefore conclude that after heat treatment, the oleic acid shell surrounding the nanoparticles constitutes the entirety of organic phase in the superlattice, while before heat treatment a ~ 7 vol% is located in the interstitial sites.

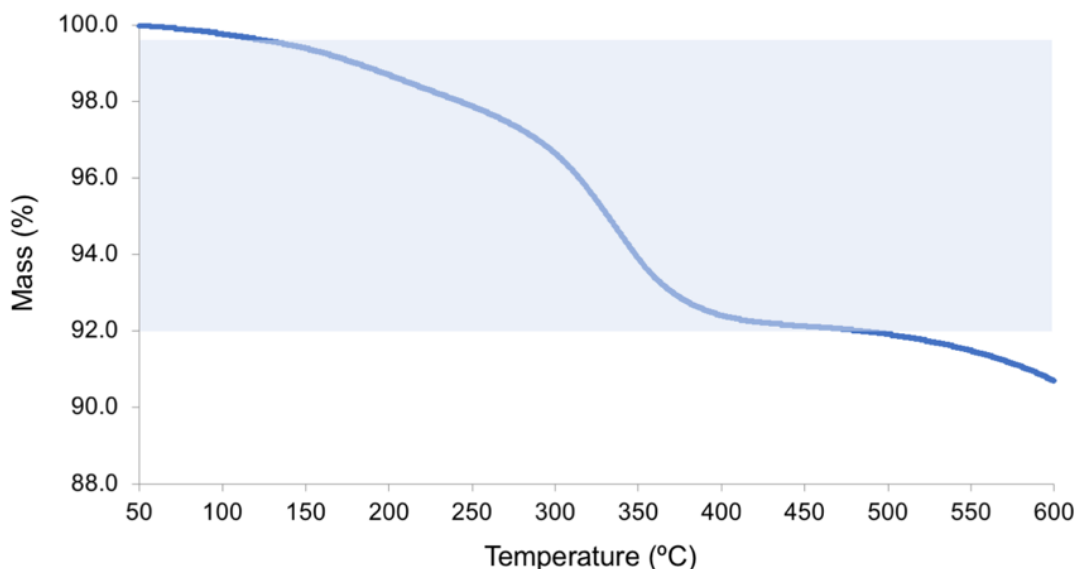


Fig. S5. Organic content. TGA curve relative to the initial dried suspension of oleic acid-functionalized iron oxide nanoparticles (in toluene). The area of interest to obtain the oleic acid content is highlighted.

5. Finite-element (FE) nanoindentation simulations

Multiscale FE simulations were implemented by defining a linear elastic behavior for the iron oxide phase, an elastic-perfectly plastic behavior for the oleic acid layer (Drucker-Prager model), and in turn an elastic-perfectly plastic behavior (also Drucker-Prager model) for the homogenized nanocomposites. Nanoindentation was numerically modelled by considering both Berkovich and cube-corner tips (diamond, linear elastic) indenting on a cylindrical ($10\ \mu\text{m}$ base radius and $10\ \mu\text{m}$ height) block of material representing the homogenized nanocomposites on the microscale, fixed at the bottom and along the lateral surface. Fig. S6 shows the study domain, and the comparison between experimental (including the scatter) and numerical data, for 300 nm indentation depth. A very good agreement is found for the Berkovich tip, also in terms of calculated hardness ($H = 4.78\ \text{GPa}$, while the experimental value is $H = 4.72\ \text{GPa}$) (35). A mismatch emerges instead for the cube-corner tip. Indeed, the numerical simulations do not include damage behavior, which plays a major role when the cube-corner tip (more acute face angle than the Berkovich) is used. Time-dependent effects are also not considered, and they are the object of ongoing work.

Fig. S7 show information additional to the graphs displayed in Fig. 2, I to K. Fig. 2 focuses on Berkovich indents with 500 nm depth, to better compare with the electron microscopy and AFM data. FEM outcomes relative to Berkovich with 300 nm depth are shown in Fig. S7, A to C, where again very good matching with AFM data on pile-ups' heights is found (see Fig. S4), and deformation patterns analogous to the 500 nm depth case are observed. Figure S7, D and E, shows the cube-corner case, 300 nm depth. Here, a difference in the pile-ups' distribution around the cube-corner indent is observed between experimental and numerical outcomes. The FE simulations show that the highest pile-ups are located at the indent's corners, which is where AFM and SEM detect cracks. This mismatch is consistent with the non-implementation of damage in the simulations.

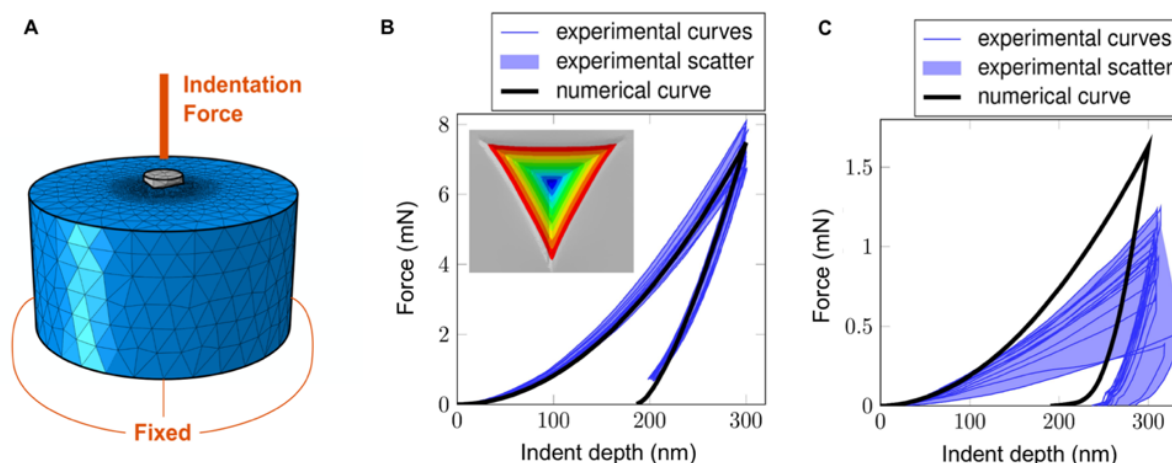


Fig. S6. Implementation of the FE nanoindentation simulations. (A) Study domain and boundary conditions. (B, C) Comparison of nanoindentation force-displacement curves, numerically and experimentally obtained, for Berkovich (B) and cube-corner (C) tips. The FE-obtained area of imprint for Berkovich tip after tip withdrawal is also plotted in (B) (sink-in scale as in Fig. S7B).

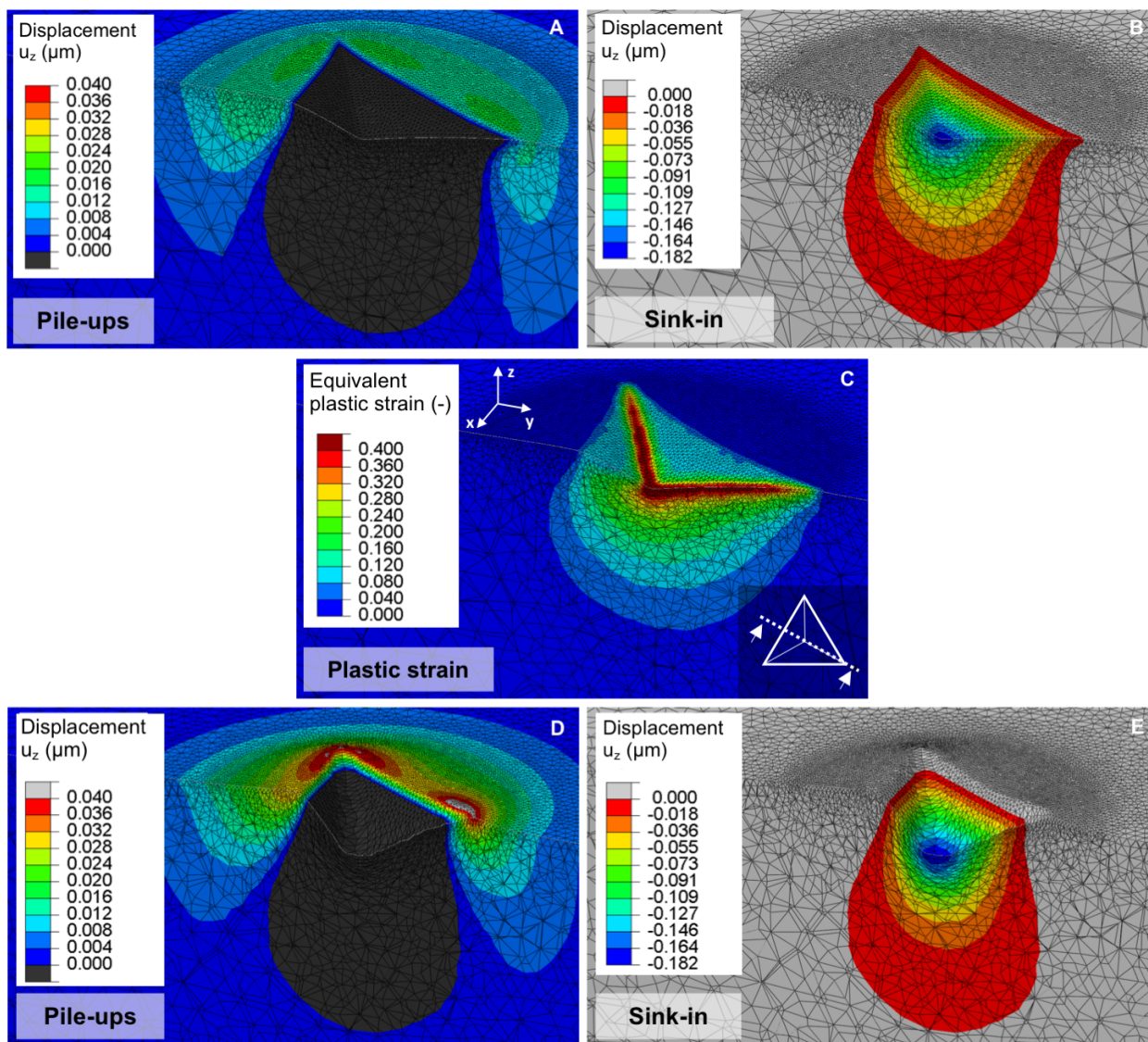


Fig. S7. FE simulations of nanoindentation tests. (A-C) 300 nm-deep Berkovich indentation: (A) pile-ups (displacements perpendicular to and above the samples' surface); (B) sink-in (displacements perpendicular to and below the samples' surface - the two plots in (A) and (B) are complementary to each other); (C) equivalent plastic strain (see Materials and Methods for definition); (D, E) 300 nm-deep cube corner indentation: (D) pile-ups (displacements perpendicular to and above the samples' surface); (E) sink-in (displacements perpendicular to and below the samples' surface - the two plots in (E) and (F) are complementary).

6. Deformed area below indents in crosslinked supercrystalline nanocomposites

Figure 3 of the main article shows a portion of the deformed area under an indent, of 500 nm depth, in the crosslinked material. Fig. S8 below shows the entire sub-indent area (A), together with the Bragg-filtering procedure adopted to highlight the plastic deformation in Fig. 3 (Fig. S8, B to D).

Another Berkovich indent, of 300 nm depth, in the crosslinked material was analyzed. Patterns analogous to the ones observed in the 500 nm case are observed (absence of pile-ups when far from the indent's center, alteration of the (111) planes orientation under the indents). Fig. S8, E to H, shows TEM/STEM (transmission and scanning transmission) images relative to this 300 nm-deep indent in the heat-treated (325 °C) material.

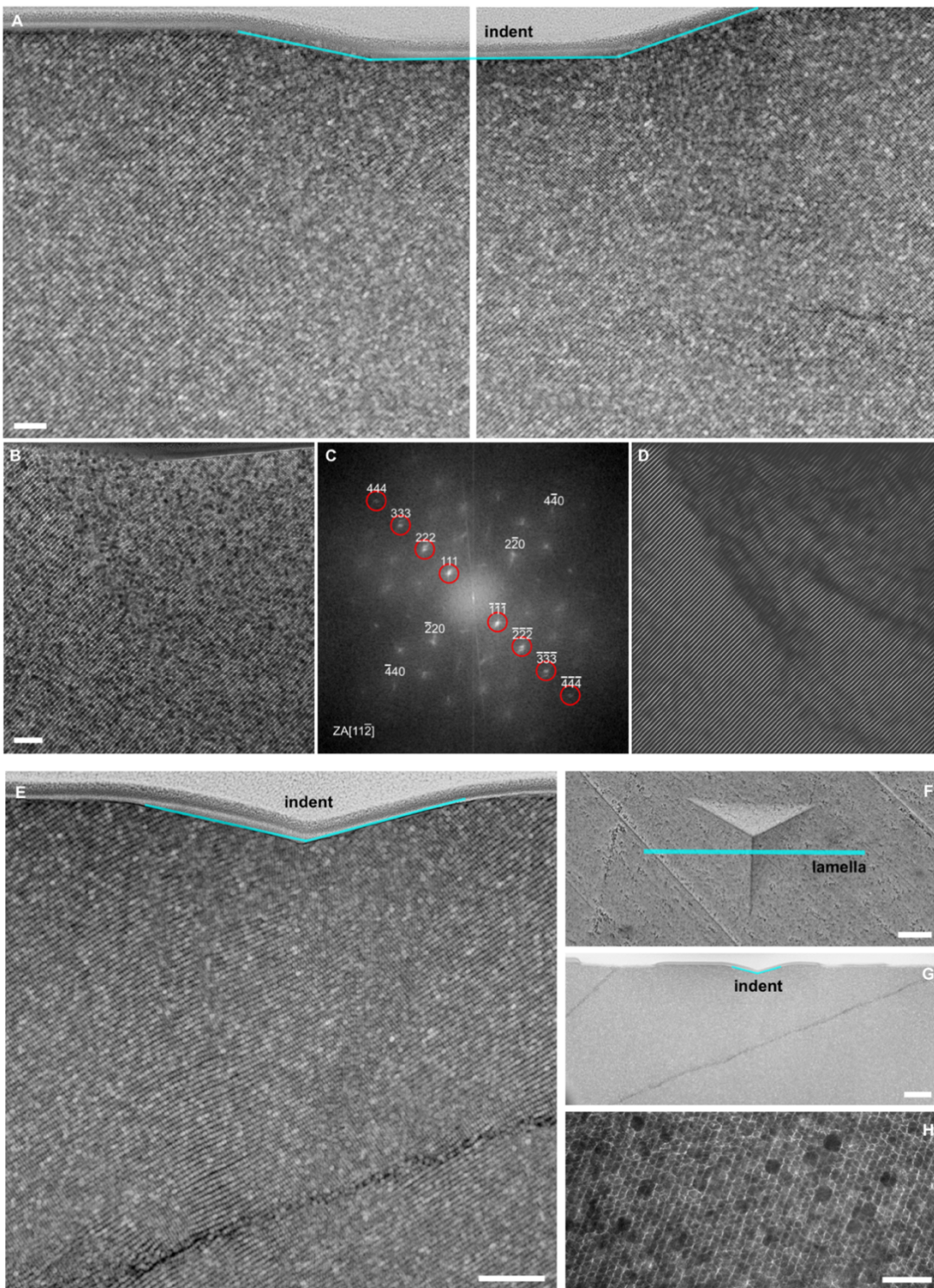


Fig. S8. Sub-indent area under indents in crosslinked nanocomposite. (A-D) 500 nm-deep indent: (A) STEM overview of the deformed area; (B) portion selected for Bragg filtering (TEM); (C) reflections used to filter from the FFT; (D) filtered image. Scale bars are 100 nm. (E-H) 300 nm-deep indent: (E) STEM overview of the altered superlattice under the indent; (F) location of the lamella with respect to the indent's center (SEM); (G) overview of the lamella (STEM), underlining how the bands/boundaries observable at some distance from the indents are not indentation-induced (the next indent is $> 30 \mu\text{m}$ away); (H) unperturbed superlattice away from indent area (TEM). Scale bars are 200, 500, 500, 50 nm.

7. Nanoindentation curves

The nanoindentation load-displacement curves relative to the lamellae shown in the main article (Fig. 3 and 4) are shown in Fig. S9. Before heat treatment, the supercrystalline nanocomposites need an applied load of 3.5 mN to reach a 500 nm depth with a Berkovich tip, while the heat-treated (crosslinked) nanocomposites need 18 mN to achieve the same indentation depth. It was verified that the creep displacement - occurring while the load is held constant - is nonlinear with time, and it is the object of current investigations. The pop-out appearing in both curves at the end of the unloading is a miscalculated thermal drift correction applied by the nanoindenter device, affected by the nonlinearity of the displacement (with respect to time) when the load is held constant (δ).

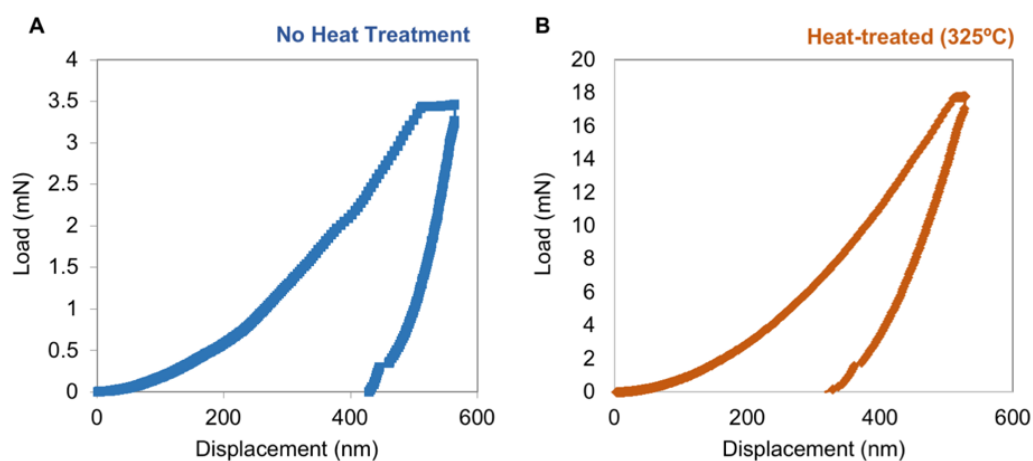


Fig. S9. Nanoindentation curves. Load-displacement curves relative to the 500-deep Berkovich indents shown in the TEM lamellae of Fig. 3 and 4 of the main article: (A) non-crosslinked material; (B) crosslinked material.